PLOS ONE

RESEARCH ARTICLE

Assessing analytical convolution effects in diffusion studies: Applications to experimental and natural diffusion profiles

Michael C. Jollands[1,2]*

1 Institute of Earth Sciences, University of Lausanne, Lausanne, Switzerland, **2** Lamont-Doherty Earth Observatory, Palisades, New York, United States of America

* jollands@ldeo.columbia.edu

Citation: Jollands MC (2020) Assessing analytical convolution effects in diffusion studies: Applications to experimental and natural diffusion profiles. PLoS ONE 15(11): e0241788. https://doi.org/10.1371/journal.pone.0241788

Editor: Marco Lepidi, University of Genova, ITALY

Received: January 24, 2020

Accepted: October 20, 2020

Published: November 24, 2020

Data Availability Statement: Codes and downloads are available www.mikejollands.com/pace and doi.org/10.5281/zenodo.4135070.

Funding: Funding P400P2_183872 from the Swiss National Science Foundation, www.snf.ch. The funders had no role in study design, data collection and analysis, decision to publish, or preparation of the manuscript.

Competing interests: The author declares that no competing interests exist.

Abstract

Given that all in-situ analytical techniques have a non-zero beam size, all measured profiles, resulting from diffusion or otherwise, will be artefactually elongated to some degree. Profiles where the total length over which the concentration changes approaches the resolution of the analytical technique likely suffer from serious convolution; the measured profiles may be considerably elongated relative to the true profile. Resolving this effect is non-trivial, except for some specific combinations of profile type and beam geometry. In this study, a versatile method for numerically deconvoluting diffusion profiles acquired using techniques with Gaussian, Lorentzian, (pseudo-)Voigt, circular/elliptical or square/rectangular interaction volumes, is presented. A MATLAB code, including a user-friendly interface (PACE-the Program for Assessing Convolution Effects in diffusion studies), is also provided, and applied to several experimental and natural profiles interpreted as resulting from diffusion, showing various degrees of convolution.

Introduction

Diffusion modelling is now commonplace in the earth sciences, given its ability to determine timescales of geological processes regardless of their absolute age [1–5]. Currently, the literature contains some open questions regarding discrepancies between different diffusion coefficients and the applicability of diffusion coefficients determined in the laboratory to natural systems. However, the effects of analytical convolution, normally artificial broadening of diffusion profiles, can, in some cases, be assessed using various analytical and numerical approaches [6–11].

The error function, which is fundamental to several analytical solutions of Fick's second law, has a geometry that corresponds to the cumulative distribution function of the normal distribution. This means that analysing a simple step function, using an analytical method where the interaction volume can be described as Gaussian, will yield an error function. Likewise, analysing an error function-shaped profile with any Gaussian beam (e.g. most analyses using nanoSIMS, electron probe, scanning electron microscope, cathodoluminescence, Fourier transform infrared spectroscopy) will lead to some smoothing-out/lengthening of the

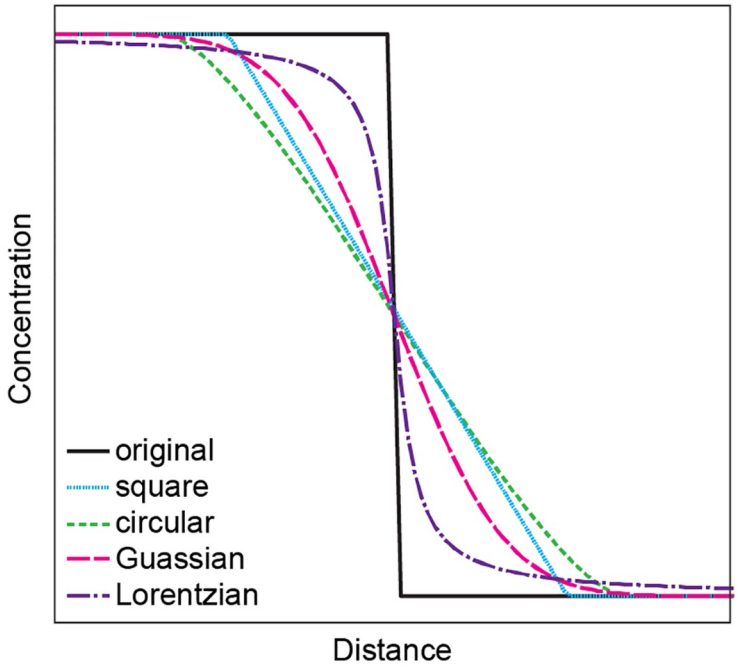

Fig 1. Types of convolution considered in this study. The pseudo-Voigt profile (not shown) is a linear combination of Gaussian and Lorentzian profiles.

https://doi.org/10.1371/journal.pone.0241788.g001

error function, whilst maintaining its form. The effect of beam convolution, in the simple case a Gaussian beam, has been derived both by Ganguly et al. and Arnould and Hild [7, 12] as:

$$D^{*}t = Dt + \sigma^{2}/2 \quad (1)$$

where D^{*} is the measured diffusion coefficient, D is the actual diffusion coefficient, σ is the standard deviation associated with a beam with a Gaussian interaction volume and t is the time for diffusion. The characteristic length of a diffusion profile is proportional to $\sqrt{(Dt)}$. From (1), the effect of convolution (($D^{*}t$)/(Dt)) is, intuitively, greatest for profiles with high σ and low Dt. Circular/elliptical, square/rectangular (e.g. laser ablation inductively coupled plasma mass spectrometry, LA-ICP-MS) and Lorentzian/(pseudo-)Voigt (some electron probe analyses) beams will also convolute profiles, with different resulting shapes (Fig 1).

Whilst this convolution effect has been recognised for several decades, it is still often omitted from diffusion studies. Therefore, to enable the fast, reproducible assessment of convolution effects, PACE (the Program for Assessing Convolution Effects in diffusion studies) is presented (Fig 2). PACE is a stand-alone package (for Mac OSX and Microsoft Windows), built in MATLAB, allowing extraction of deconvoluted profiles from measured profiles where 1) circular, square, Gaussian, Lorentzian or pseudo-Voigt interaction volumes can be assumed; 2) where the beam size is known *a priori*, or can be estimated and 3) where an assumption can be made regarding the true nature, i.e. the geometry, of the profile. A second program-PACE-IC (PACE-Initial Conditions) is also provided, this is based on PACE, but allows the user to input initial and boundary conditions. In addition, a third program—PACE-GD (Get Dimensions) is provided for estimating beam sizes from profiles made across known step functions, with any of the interaction types listed above.

The software does not assume knowledge of programming or diffusion past simple recognition of profile types. The use of PACE is demonstrated on several diffusion profiles with

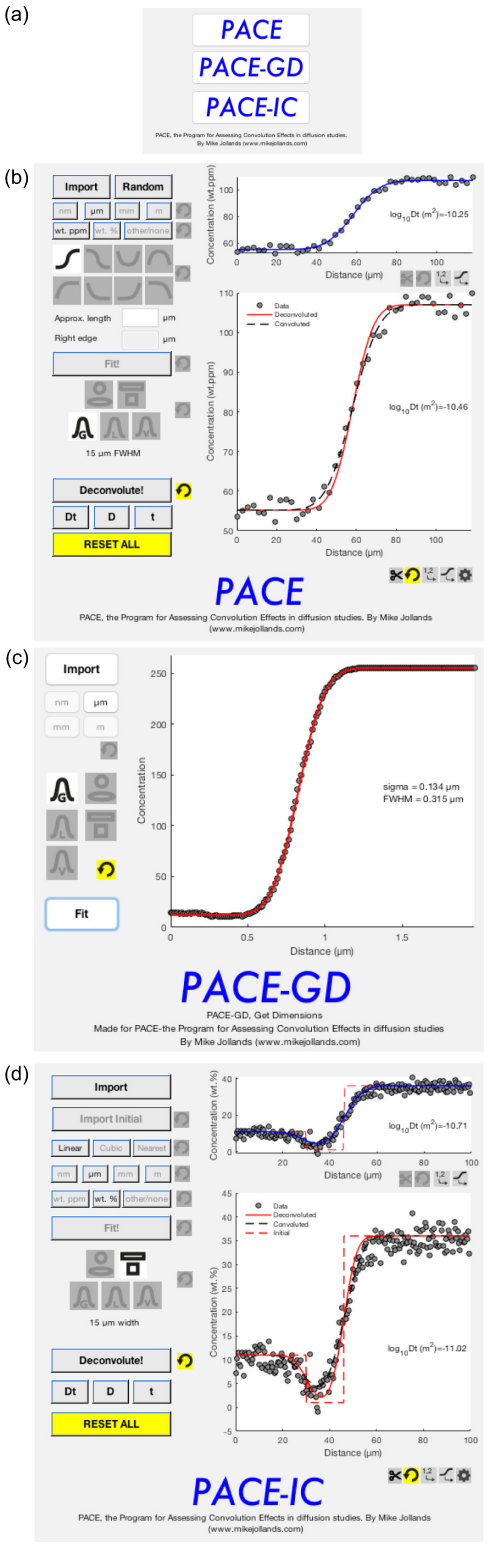

Fig 2. Screenshots from PACE, PACE-GD and PACE-IC. (a) shows the start screen, from which the others are accessed. (b) is the main screen from PACE, following fitting and deconvolution of a random profile. The top right hand panel shows the initial fit (blue line) to the data (points), then the lower panel shows the deconvoluted (solid red line) and convoluted (dashed black line) fits, incorporating a Gaussian beam with a 15 µm full width at half-maximum (c) shows PACE-GD following extraction of a beam size from a Gaussian convoluted profile. (d) shows PACE-IC

following fitting and deconvolution of a profile with a stepped initial condition, and a 15 μm wide square/rectangular beam. The top panel shows the initial fit using the imported initial condition (red dashed line), then the deconvoluted profile, as in (b).

https://doi.org/10.1371/journal.pone.0241788.g002

different beam geometries, showing both cases where the convolution effects are negligible, and where they may become important.

Methods

Solutions to Fick's second law (PACE)

The methodology used in PACE only employs analytical solutions to the diffusion equation—it does not incorporate any numerical diffusion modelling. Therefore, PACE can only be used in cases where the boundary conditions are fixed, and the initial conditions are describable using step functions. Numerical modelling is incorporated into PACE-IC (described below). This precludes the use of PACE in certain situations including 1) changing temperature, leading to partition/distribution coefficients changing over time and 2) loss of the original core composition following a prolonged period of diffusion.

For simulating sigmoidal shaped profiles that include flat plateaus on the left and right, eq (2) is used:

$$C(x,t) = C_2 + (C_1\text{-}C_2) \times \frac{1}{2} \times \mathrm{erfc}\left(\frac{x\text{-}X}{2\sqrt{Dt}}\right) \quad (2)$$

Where C(x,t) is the concentration at position x and time t, X is the midpoint/inflection point of the profile and D is the diffusion coefficient (m^2s^{-1}).

For U and upside-down-U shaped profiles, eq (3) is used:

$$C(x,t) = C_2 + (C_1\text{-}C_2) \times \left(\mathrm{erfc}\left(\frac{x}{2\sqrt{Dt}}\right) + \mathrm{erfc}\left(\frac{X\text{-}x}{2\sqrt{Dt}}\right)\right) \quad (3)$$

where in this case, C_1 and C_2 represent boundary and core concentrations, and X is the length of the system, i.e. the position of the right-hand boundary, where the left-hand boundary is at x = 0 by default.

For profiles where the boundary is at x = 0 (left hand side) and the system is considered semi-infinite, eq (4) is used:

$$C(x,t) = C_2 + (C_1\text{-}C_2) \times \mathrm{erfc}\left(\frac{x}{2\sqrt{Dt}}\right) \quad (4)$$

and where the boundary is on the right-hand side of the profile at $x \neq 0$, again in a semi-infinite system, eq (5) is used instead:

$$C(x,t) = C_2 + (C_1\text{-}C_2) \times \mathrm{erfc}\left(\frac{X\text{-}x}{2\sqrt{Dt}}\right) \quad (5)$$

where X is again the position of the boundary. By default, PACE outputs $\log_{10}Dt$, along with the respective concentrations. From this, D or t can be readily extracted when the other is known, or, because $Dt = \int D(t)dt$ [13], Dt can also be used to extract cooling histories.

Numerical diffusion modelling (PACE-IC)

PACE-IC uses an explicit finite difference method to solve Fick's second law numerically in one dimension. This method is described thoroughly elsewhere [14–16], but, briefly, the

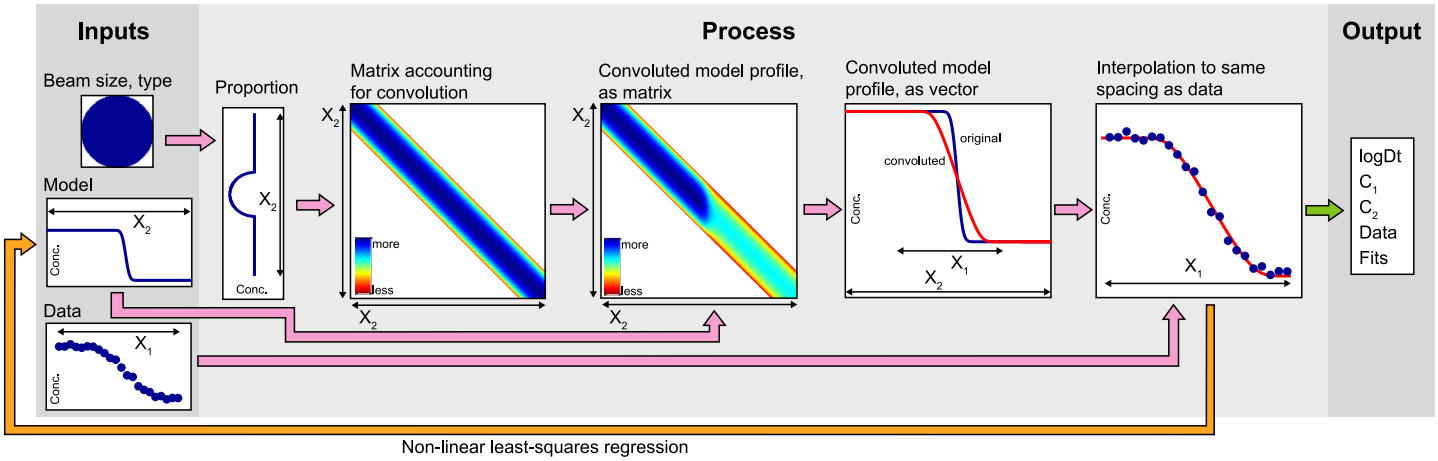

Fig 3. Method for convoluting diffusion profiles, described in the text.

https://doi.org/10.1371/journal.pone.0241788.g003

system is modelled as a vector representing a series of equidistant steps (spacing = Δx), with the initial and boundary conditions imported by the user. The model then steps forwards through time (size of time step = Δt), with the concentration (C) at each distance step (i) recalculated at every time step (j):

$$C_{i,j+1} = C_{i,j} + D\Delta t\left(\frac{C_{i+1,j}\text{-}2C_{i,j}+C_{i-1,j}}{\Delta x^2}\right) \quad (6)$$

The size of the time step is defined by D and Δx, $(D\Delta t)/\Delta x^2$ must be less than 0.5 for stability. PACE-IC assumes that the boundaries are constant over time.

Simulating beam convolution

A workflow describing how beam convolution is simulated in PACE is presented in Fig 3, with the methodology described herein.

The inputs are 1) details regarding the nature of the beam; 2) a model profile vector, which is generated from the non-linear least squares regression and 3) the measured profile, i.e. the data vector, which may or may not include uncertainties. The model profile vector is longer than the data vector, in that it extends past the highest and lowest distance values. This is shown in the 'Inputs' section of Fig 3 –the data vector has a total length X_1, and the model profile vector has length X_2, where $X_2 > X_1$.

To simulate convolution, a square matrix is constructed (denoted 'Matrix accounting for convolution' in Fig 3), with dimensions X_2 by X_2. This is a matrix of zeros, with each column and row containing a vector representing the sampling density associated with a given beam type and size (shown as 'Proportion' in Fig 3). Notably, this calculation assumes uniform sampling density when using circular/elliptical and square/rectangular beams. For LA-ICP-MS analyses, this means flat-bottomed craters with vertical walls, which is a reasonable assumption for modern systems (e.g. Fig 1 of Neymark et al. [17]).

The matrix accounting for convolution is then multiplied by the model profile vector pointwise. This gives a new matrix, denoted 'Convoluted model profile, as matrix' in Fig 3.

This matrix is then summed along one dimension to form a vector, denoted 'Convoluted model profile, as vector' in Fig 3. The vector is then interpolated to find the nearest points to the data, and the difference between this vector and the data is minimised using the *lsqnonlin* solver in MATLAB. Whilst obviously slower computationally than the analytical solution for

deconvoluting the effect of a Gaussian beam on an error function [7], this method is versatile—it can potentially be used for simulating any beam shape and any profile shape, as long as an assumption can be made regarding the nature of, i.e. the true form of, the deconvoluted profile.

Treatment of boundaries

In order to simulate convolution, it is necessary to begin with a profile that is longer than the measured profile. In the case of the curves generated by eq (2), where the extremities of the curve are flat segments, the boundaries are simply extended. However, where the curve intersects a boundary with constant composition (e.g. eqs (3)–(5)), the situation is slightly more complex. In PACE, the boundaries in these equations are considered as fixed. This means that the convolution effect becomes smaller towards the boundary, i.e., in the most extreme case, a point made exactly at the boundary using a Gaussian beam will only be convoluted by the inside of the crystal, and not the outside. Whilst not ideal, the other options are 1) adding a flat segment outside of the boundary, which leads to a slight sigmoidal shape at the boundary after convolution and 2) continuing the curve outside of the boundary, which is physically unrealistic.

Estimating beam size

Where circular/elliptical or square/rectangular beams are used, the beam size is either known, or can be directly measured from photomicrographs. Otherwise, the beam size can be determined using a profile measured over a known step function, either real or simulated.

The diameter of a circular beam can be obtained from a profile made over a known step function by approximately running the methodology presented in Fig 3 in reverse. The width of a square or rectangular beam is determined by calculating a moving mean from a step function, then calculating the window size necessary for fitting the moving mean to the data representing a convoluted known step function, which should be three linear segments.

Likewise, where the beam is Gaussian, Lorentzian or Voigt, the size can be estimated or directly measured. For a Gaussian beam, a measured profile over a step function is fitted to an equation with the form:

$$C(x) = C_2 + (C_1\text{-}C_2) \times \frac{1}{2}\left(1 + \mathrm{erf}\left(\frac{x\text{-}X}{\sqrt{2}\sigma}\right)\right) \tag{7}$$

and for a Lorentzian beam:

$$C(x) = C_2 + (C_1\text{-}C_2) \times \left(\frac{1}{\pi}\arctan\left(\frac{x\text{-}X}{\gamma}\right) + \frac{1}{2}\right) \tag{8}$$

C_1, C_2, x and X have the same meanings as in eq (2). For the Gaussian (G), the full width at half maximum (FWHM, Γ) is $2\sqrt{(2\ln 2)}\sigma$, and $\Gamma = 2\gamma$ for the Lorentzian (L). For beams best approximated by Voigt shapes, pseudo-Voigt (pV) profiles are simulated from a linear combination of (7) and (8):

$$C(x, \Gamma)_{[pV]} = \eta C(x, \Gamma)_{[G]} + (1\text{-}\eta) C(x, \Gamma)_{[L]} \tag{9}$$

[18]. FWHM (Γ) of the pseudo-Voigt ($\Gamma_{[pV]}$) line is determined from those of the Gaussian ($\Gamma_{[G]}$) and Lorentzian ($\Gamma_{[L]}$) lines:

$$\begin{aligned}\Gamma_{[pV]} = (&\Gamma_{[G]}^5 + 2.69269\Gamma_{[G]}^4\Gamma_{[L]} + 2.42843\Gamma_{[G]}^3\Gamma_{[L]}^2 + 4.47163\Gamma_{[G]}^2\Gamma_{[L]}^3 \\ &+0.07842\Gamma_{[G]}\Gamma_{[L]}^4 + \Gamma_{[L]}^5)^{\frac{1}{5}}\end{aligned} \tag{10}$$

and η is estimated as:

$$\eta = 1.36603\left(\frac{\Gamma_{[G]}}{\Gamma_{[pV]}}\right) - 0.47719\left(\frac{\Gamma_{[L]}}{\Gamma_{[pV]}}\right)^2 + 0.11116\left(\frac{\Gamma_{[L]}}{\Gamma_{[pV]}}\right)^3 \quad (11)$$

[19]. All of the above methods are incorporated into PACE-GD.

Where a profile over a couple with a perfect step function, either experimental or natural, cannot be directly measured, software packages allow the direct simulation of electron interactions and thus the extraction of beam size (e.g. CASINO [20]). For example, consider a case where Fe-Mg profiles are measured by electron microprobe (e.g. [21–24]. A couple between Fo_{85} and Fo_{90} (i.e. Mg/(Mg+Fe) = 0.85 and 0.90, respectively) was simulated using CASINO v2 at a series of accelerating voltages, then the resulting profiles fitted using PACE-GD, both assuming a Gaussian beam and assuming a pseudo-Voigt shape. According to the simulation, the assumption of a Gaussian interaction is valid up to ~15 kV, after which the interaction develops wider tails and becomes more Lorentzian in shape, reflected in the relative FWHMs of the Lorentzian and Gaussian components of the pseudo-Voigt interaction volumes (Fig 4). The advantage of the empirical deconvolution method shown in Fig 3 is that any such interaction type can be simulated, without the requirement that the interaction volume is strictly Gaussian, as required when using eq (1).

Aside from convolution effects associated with interaction volumes, there are also effects associated with secondary fluorescence in EPMA. This is associated with measuring low concentrations of elements in phases adjacent to a phase with a much higher concentration of the same element [25, 26], such as Ti in quartz adjacent to rutile [27]. The method in PACE does not account for this phenomenon. The extent of this effect will be sample specific, and specific to the analytical conditions used.

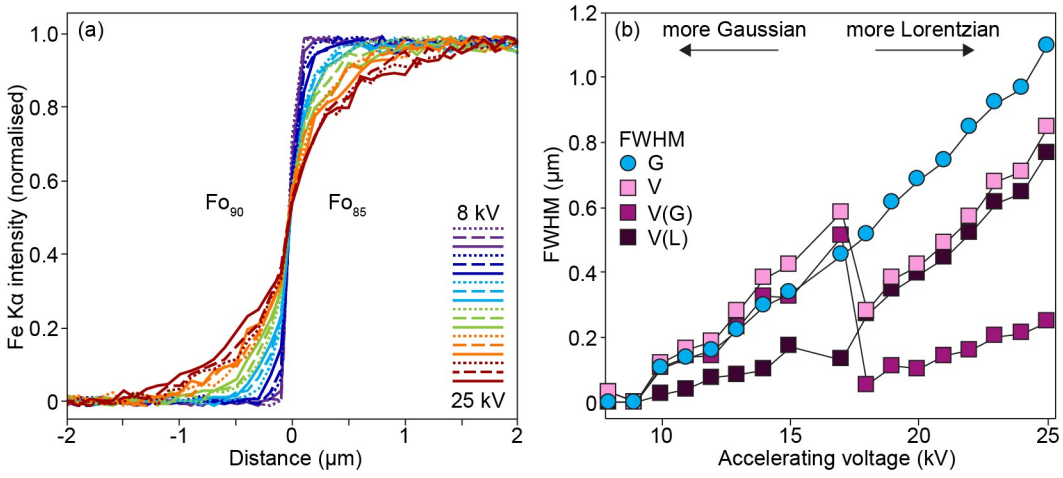

Fig 4. The effect of EPMA accelerating voltage on a step function measured over a Fo_{85}-Fo_{90} couple, simulated using the Monte Carlo method implemented in CASINO (20). (a) profiles of Fe Kα (counts, normalised) as a function of accelerating voltage, showing an increase in width, but also a change in shape, as the kV increases. (b) the profiles from (a), deconvoluted using PACE-GD to give the FWHM as a function of kV. This was done both assuming a purely Gaussian interaction (circles) as well as a pseudo-Voigt interaction (squares). The FWHM of the pseudo-Voigt line is shown (V), as well as those of the Gaussian (V(G)) and Lorentzian (V(L)) components comprising the Voigt line. Lines (dashed, dotted and solid) represent increasing intervals of 1 kV.

https://doi.org/10.1371/journal.pone.0241788.g004

Example applications

These tools have applicability both where experimental diffusion profiles are measured (e.g. in experimental petrology, materials science) and for natural diffusion profiles (often measured in petrology, volcanology, etc). Some example applications are presented below.

Experimental Ti diffusion profiles in quartz

Ti diffusion in quartz has had wide ranging applications, including determining timescales of 1) magma chamber processes [3, 28–30]; 2) metamorphic cycles [31] and 3) porphyry formation [32], as well as for proposing a relatively low granite solidus [33]. Therefore, the accurate determination of Ti diffusivities in quartz is of considerable importance.

Fig 5 shows cathodoluminescence images of two quartz pieces, both including a low Ti core (<0.2 wt. ppm) over which a high Ti rim (~3000 wt. ppm) was grown experimentally (both images courtesy of Andreas Audétat at the Bayerisches Geoinstitut, Germany). The couple in Fig 5a shows the sample directly after synthesis (1000˚C, 1 kbar, 5 hours). The couple in Fig 5b shows the same sample after annealing at 1600˚C, 20 kbar, for 89.5 h, to induce diffusive Ti flux. Fitting eq (7) to five grayscale profiles extracted (using ImageJ [34]) from the interface between the high and low Ti sections of the non-annealed couple (Fig 5a) gives a mean σ = 137 nm, hence FWHM = 322 nm (determined by PACE-GD). Applying the same FWHM to a profile extracted from the annealed couple gives $\log_{10}$Dt (m^2) = -13.41(±0.01) (deconvoluted),

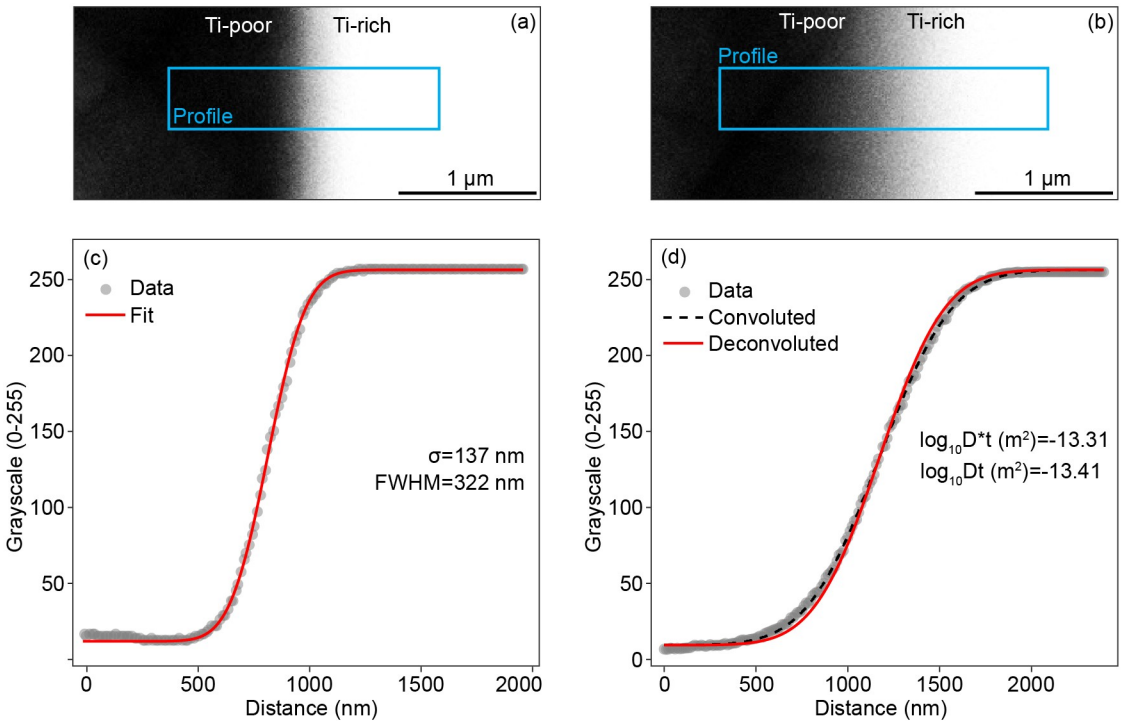

Fig 5. Deconvoluting Ti profiles in quartz determined by SEM-CL. Images were acquired using a Zeiss Gemini 1530 field emission gun scanning electron microscope equipped with an ellipsoidal mirror and an ASK SEM-CL View VIS (250–900 nm) imaging spectrometer. The SEM was operated at 7 kV, 10 nA with a working distance of 14.2 mm. (a) CL image of an un-annealed high Ti quartz-low Ti quartz couple, with an extracted greyscale profile in (c). (b), same sample as in (a), after annealing at 1600˚C, 20 kbar for 89.5 h, showing a wider transition zone, with the extracted profile in (d). (c) assuming that the gradient in (a) is purely convolution (i.e. (a) is a step function) and the beam-sample interaction is Gaussian, the FWHM is determined by fitting a curve with the form erf(x/($\sqrt{2}\sigma$)) to the data, giving FWHM = 322 nm. (d) extracted profile from (b), deconvoluted using PACE and the FWHM from (c). The 'Ti-rich' section contains ~3000 wt. ppm Ti, versus <0.2 wt ppm for the 'Ti-poor' section.

https://doi.org/10.1371/journal.pone.0241788.g005

with the original fit giving $\log_{10}D^{*}t$ (m^2) = -13.31(±0.01). As t = 89.5 h, $\log_{10}t$ (s) = 5.51 so $\log_{10}D$ (m^2s^{-1}) = -18.92. Interestingly, this diffusion coefficient is lower than extrapolations of both previous experimental determinations of Ti diffusion in quartz [35, 36]. This could be an effect of pressure, composition or diffusion mechanism, but this does not affect the validity of the deconvolution routine.

Magmatic timescales from the Bishop Tuff

Volcanic quartz crystals often preserve zoning in Ti content, interpreted to be formed by changes in titania activity or temperature, or be the consequence of disequilibrium during growth [37–41]. In any case, the Ti zoning leads to intra-crystalline chemical potential gradients, which drive diffusive flux. The spatial extent of the diffusion profiles can then be used to understand the temperature-time history of the magmatic system. Gualda et al. [42] presented 20–30 μm long profiles measured using synchrotron X-ray microfluorescence with a stated 5 μm beam size, assumed to represent the FWHM of a Gaussian beam-sample interaction (e.g. [43]). Applying PACE to their data shows a minor convolution effect, resulting in a Dt shift of 0.06 log units, which equates to a time decrease of just ~13%. This effect can be considered negligible given reasonable uncertainties associated with diffusion modelling, which, for this system, mainly include 1) temperature; 2) whether samples are prepared with a plane exactly perpendicular to the compositional boundary; 3) discrepancies between experimental determinations of diffusion coefficients [35, 36] and 4) initial conditions.

In this case, given the profile and beam types, the result can be compared to the exact formulation in eq (1), which gives $\log_{10}D^{*}t$ (m^2) = -10.86 (c.f. -10.87 in Fig 6). The former is exact, whereas the latter is a numerical approximation, hence the small discrepancy.

Experimental diffusion profiles measured using a rectangular laser beam

Slit-shaped beams are now routinely used in laser ablation inductively-coupled plasma mass spectrometry (LA-ICP-MS) to measure concentration profiles in minerals and glasses [44–47].

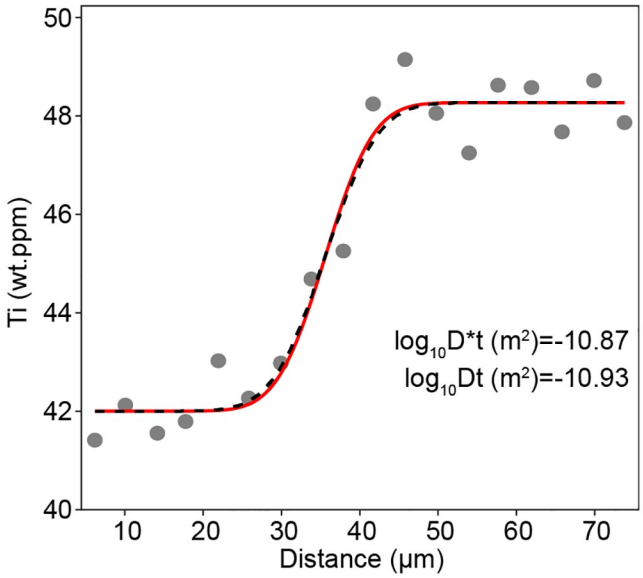

Fig 6. Data from Gualda et al [42], fitted and deconvoluted using PACE, assuming a 5 μm FWHM Gaussian beam. The measured Dt ($D^{*}t$) is just 0.06 log units greater than the true Dt (Dt), i.e. convolution has almost no effect on the measured profile.

https://doi.org/10.1371/journal.pone.0241788.g006

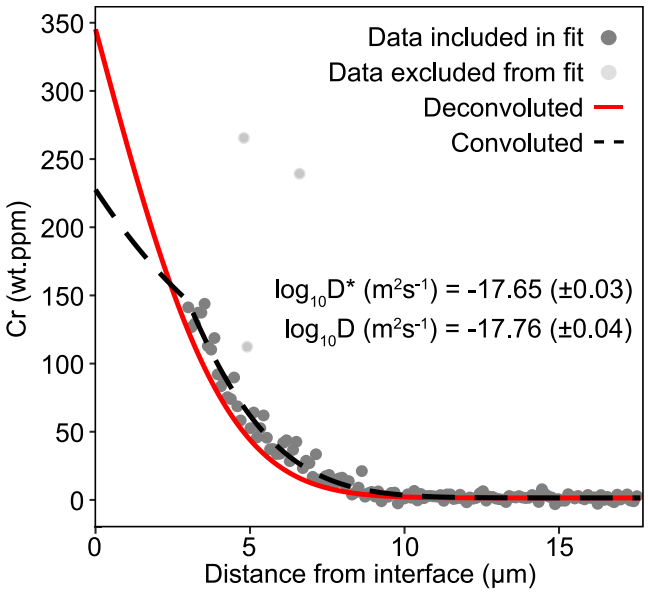

Fig 7. An experimental Cr diffusion profile in forsterite, measured using LA-ICP-MS with a 6x100 μm, deconvoluted. The measured D (D^*) is 0.11 log units higher than the deconvoluted D. Note the deviation between data and model in the near-interface region—this is due to the way that PACE treats boundaries (fixed composition equal to the rim composition).

https://doi.org/10.1371/journal.pone.0241788.g007

In this technique, a slit-shaped aperture is placed in the optical pathway and rotated to have its long axis parallel to the diffusion interface. The sample is then moved beneath the stationary beam, continuously passing data to a mass spectrometer, creating a profile of concentration versus distance. Jollands et al. [47] presented an experimental data set of Cr diffusion in olivine measured in this manner. The diffusivity of Cr was shown to be highly anisotropic in olivine, with considerably higher diffusivity parallel to [1] than [100], and also dependent on the externally-buffered silica activity, with higher silica activity giving higher diffusivities. Together, profiles measured parallel to [100] following low silica activity experiments were often short, which in this case means <10 μm. One such profile is shown in Fig 7, with a ~9 μm long Cr diffusion profile, measured using a 6 μm wide (by 100 μm long) laser beam. This was following an experiment at 1306˚C, for ~35 days. The convoluted $\log_{10}D^*$ (m^2s^{-1}) = -17.65 ± 0.03. Following deconvolution (Fig 7), $\log_{10}D$ (m^2s^{-1}) = -17.76 ± 0.04, resolvably different from the convoluted data. The advantage with this method is that, because the length scale of a diffusion profile is broadly proportional to the square root of time, if such short profiles can be deconvoluted, then this opens up the possibility for running shorter experiments and/or experiments at relatively low temperatures.

Experimental Pb in zircon profiles measured by EPMA

An accurate determination of the diffusivity of Pb in zircon is essential for determining the closure temperature associated with U-Pb dating. Cherniak and Watson [48] presented a profile of Pb-out diffusion from zircon measured by EPMA to supplement a large dataset of Pb diffusivities measured by Rutherford Backscattering Spectroscopy. The measured profile was ~6 μm long, measured with a 25 kV beam. A CASINO simulation of a line profile measured at 25 kV, over a high Pb—low Pb zircon couple gives an error function form (i.e. a Gaussian beam) with σ = 693 nm, i.e. FWHM = 1633 nm. However, because Cherniak and Watson [48] measured on a section 30˚ from obliquity with the diffusion interface, the interaction volume

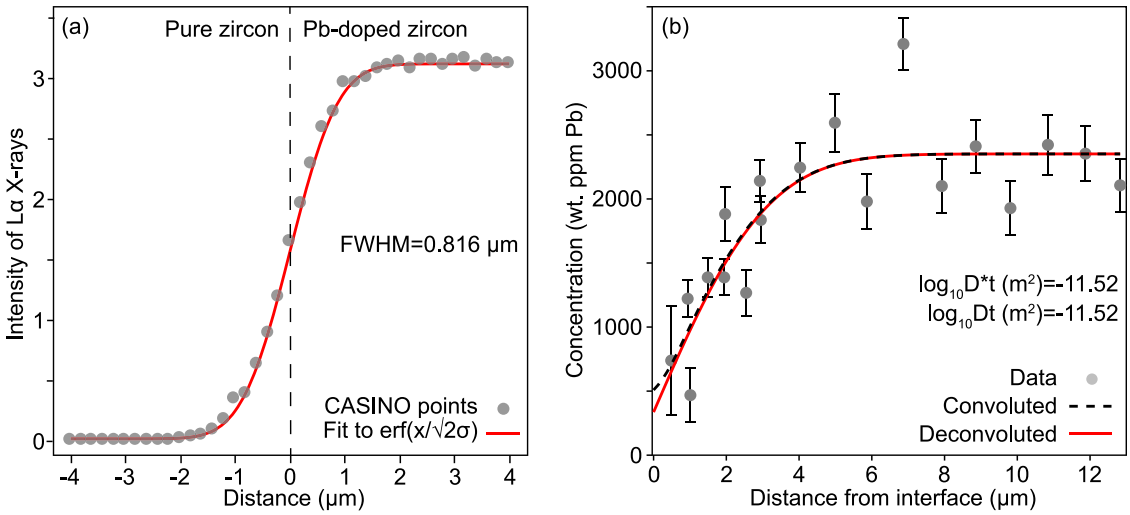

Fig 8. Deconvoluting a Pb in zircon profile from [48]. (a) shows an apparent Pb Lα profile between Pb-doped and Pb-free zircon, generated by CASINO [20], using an incident beam at 25 kV with a nominal 2 μm diameter. From the fit, σ = 693 nm, hence FWHM = 1633 nm. However, because [48] analysed a section 30˚ from normal to the interface, the relevant FWHM is 1633/~2 ≈ 816 nm. (b) shows the [48] EPMA profile, deconvoluted. Convolution has an effect of <0.01 $\log_{10}$D units in this case.

https://doi.org/10.1371/journal.pone.0241788.g008

is compressed by approximately a factor of two in the direction of diffusion. Thus, a FWHM of 816 nm was used for deconvolution.

Deconvoluting the measured profile (Fig 8) shows that the effect of artificial profile lengthening is only 0.01 $\log_{10}$Dt units in this case, far smaller than the uncertainty from curve fitting. That this effect is so small, even when using a 25 kV beam, is due to a combination of the high stopping power of zircon and the measurements having been done on a non-oblique section.

Concluding remarks

The PACE software packages allow rapid, simple determinations of analytical convolution artefacts associated with measuring diffusion profiles, either experimental or natural. Whilst the majority of experimental and natural profiles are comfortably much longer than the beam size used to measure them, profiles approaching analytical spatial resolution are becoming more common in the literature. PACE simplifies the extraction of quantitative data from such profiles, and also enables a rapid *diffusion profile* versus *no measurable diffusion profile* distinction to be made. Such tools will become more important as diffusion modelling is used to determine increasingly short timescales.

Supporting information

S1 File.
(ZIP)

S2 File.
(ZIP)

S3 File.
(PDF)

S4 File.
(ZIP)

Acknowledgments

Thanks go to Andreas Audétat for generously providing CL images of experimental quartz couples. Three anonymous reviewers are thanked for comprehensive comments and suggestions that helped to clarify the manuscript, and strengthen the software. Marco Lepidi is thanked for editorial handling. Any ideas and suggestions of ways in which to improve the functionality and/or user-friendliness of PACE will be greatly appreciated.

Author Contributions

Conceptualization: Michael C. Jollands.

Formal analysis: Michael C. Jollands.

Funding acquisition: Michael C. Jollands.

Investigation: Michael C. Jollands.

Methodology: Michael C. Jollands.

Project administration: Michael C. Jollands.

Resources: Michael C. Jollands.

Software: Michael C. Jollands.

Validation: Michael C. Jollands.

Visualization: Michael C. Jollands.

Writing – original draft: Michael C. Jollands.

Writing – review & editing: Michael C. Jollands.

References

1. Peslier AH, Woodland AB, Wolff JA. Fast kimberlite ascent rates estimated from hydrogen diffusion profiles in xenolithic mantle olivines from southern Africa. Geochimica et Cosmochimica Acta. 2008; 72 (11):2711–22.
2. Ruprecht P, Plank T. Feeding andesitic eruptions with a high-speed connection from the mantle. Nature. 2013; 500(7460).
3. Wark DA, Hildreth W, Cherniak DJ, Watson EB, Spear FS. Pre-eruption recharge of the Bishop magma system. Geology. 2007; 35(3):235–8.
4. Chakraborty S. Diffusion in solid silicates: A tool to track timescales of processes comes of age. Annu Rev Earth Pl Sc. 2008; 36.
5. Costa F, Morgan D. Time constraints from chemical equilibration in magmatic crystals. 2011.
6. Bradshaw RW, Kent AJR. The analytical limits of modeling short diffusion timescales. Chemical Geology. 2017; 466:667–77.
7. Ganguly J, Bhattacharya R, Chakraborty S. Convolution effect in the determination of compositional profiles and diffusion coefficients by microprobe step scans. American Mineralogist. 1988; 73:901–9.
8. Jones AF, Misell DL. A practical method for the deconvolution of experimental curves. British Journal of Applied Physics. 1967; 18(10):1479–83.
9. Goldstein J, Colby J. Special techniques in the X-ray analysis of samples. Practical Scanning Electron Microscopy: Springer; 1975. p. 435–89.
10. Lo C, Schuele D. Beam-diameter correction of x-ray intensity profile over small diffusion zones. Journal of Applied Physics. 1975; 46(11):5004–9.
11. Zhukova I, O'Neill H, Campbell IH, Fiorentini M, Kilburn M, Guagliardo P. Diffusion and solubilities of Rh, Ru and Ir in olivine and spinel. Chemical Geology. 2018; 494:19–29.
12. Arnould O, Hild F. EPMA measurements of diffusion profiles at the submicrometre scale. Microchimica Acta. 2002; 139(1–4):3–10.

13. Ganguly J. Diffusion kinetics in minerals: principles and applications to tectono-metamophic processes. 2002.

14. Costa F, Dohmen R, Chakraborty S. Time scales of magmatic processes from modeling the zoning patterns of crystals. Reviews in Mineralogy and Geochemistry. 2008; 69(1):545–94.

15. Crank J. The Mathematics of Diffusion. Oxford: Oxford University Press; 1975.

16. Smith GD, Smith GD, Smith GDS. Numerical solution of partial differential equations: finite difference methods: Oxford university press; 1985.

17. Neymark LA, Holm-Denoma CS, Moscati RJ. In situ LA-ICPMS U—Pb dating of cassiterite without a known-age matrix-matched reference material: Examples from worldwide tin deposits spanning the Proterozoic to the Tertiary. Chemical Geology. 2018; 483:410–25.

18. Ida T, Ando M, Toraya H. Extended pseudo-Voigt function for approximating the Voigt profile. Journal of Applied Crystallography. 2000; 33(6):1311–6.

19. Thompson P, Cox DE, Hastings JB. Rietveld refinement of Debye-Scherrer synchrotron X-ray data from Al2O3. Journal of Applied Crystallography. 1987; 20(2):79–83.

20. Hovington P, Drouin D, Gauvin R. CASINO: A new Monte Carlo code in C language for electron beam interaction—Part I: Description of the program. Scanning. 1997; 19(1):1–14.

21. Hartley ME, Morgan DJ, Maclennan J, Edmonds M, Thordarson T. Tracking timescales of short-term precursors to large basaltic fissure eruptions through Fe—Mg diffusion in olivine. Earth and Planetary Science Letters. 2016; 439:58–70.

22. Shea T, Lynn KJ, Garcia MO. Cracking the olivine zoning code: Distinguishing between crystal growth and diffusion. Geology. 2015; 43(10):935–8.

23. Gordeychik B, Churikova T, Kronz A, Sundermeyer C, Simakin A, Wörner G. Growth of, and diffusion in, olivine in ultra-fast ascending basalt magmas from Shiveluch volcano. Scientific Reports. 2018; 8 (1):11775. https://doi.org/10.1038/s41598-018-30133-1 PMID: 30082716

24. Girona T, Costa F. DIPRA: A user-friendly program to model multi-element diffusion in olivine with applications to timescales of magmatic processes. Geochemistry, Geophysics, Geosystems. 2013; 14 (2):422–31.

25. Llovet X, Galan G. Correction of secondary X-ray fluorescence near grain boundaries in electron microprobe analysis: Application to thermobarometry of spinel lherzolites. American Mineralogist. 2003; 88 (1):121–30.

26. Dalton JA, Lane SJ. Electron microprobe analysis of Ca in olivine close to grain boundaries: the problem of secondary X-ray fluorescence. American Mineralogist. 1996; 81(1–2):194–201.

27. Sato K, Santosh M. Titanium in quartz as a record of ultrahigh-temperature metamorphism: the granulites of Karur, southern India. Mineralogical Magazine. 2007; 71(2):143–54.

28. Matthews NE, Huber C, Pyle DM, Smith VC. Timescales of Magma Recharge and Reactivation of Large Silicic Systems from Ti Diffusion in Quartz. Journal of Petrology. 2012; 53(7):1385–416.

29. Saunders KE, Morgan DJ, Baker JA, Wysoczanski RJ. The Magmatic Evolution of the Whakamaru Supereruption, New Zealand, Constrained by a Microanalytical Study of Plagioclase and Quartz. Journal of Petrology. 2010; 51(12):2465–88.

30. Wiebe RA, Wark DA, Hawkins DP. Insights from quartz cathodoluminescence zoning into crystallization of the Vinalhaven granite, coastal Maine. Contributions to Mineralogy and Petrology. 2007; 154(4):439–53.

31. Spear FS, Wark DA. Cathodoluminescence imaging and titanium thermometry in metamorphic quartz. Journal of Metamorphic Geology. 2009; 27(3):187–205.

32. Mercer CN, Reed MH, Mercer CM. Time Scales of Porphyry Cu Deposit Formation: Insights from Titanium Diffusion in Quartz. Economic Geology. 2015; 110(3):587–602.

33. Ackerson MR, Mysen B, Tailby N, Watson E. Low-temperature crystallization of granites and the implications for crustal magmatism. Nature. 2018; 559(7712):94. https://doi.org/10.1038/s41586-018-0264-2 PMID: 29950721

34. Schindelin J, Rueden CT, Hiner MC, Eliceiri KW. The ImageJ ecosystem: An open platform for biomedical image analysis. Molecular Reproduction and Development. 2015; 82(7–8):518–29. https://doi.org/10.1002/mrd.22489 PMID: 26153368

35. Jollands MC, Bloch E, Müntener O. New Ti-in-quartz diffusivities reconcile natural Ti zoning with time scales and temperatures of upper crustal magma reservoirs. Geology. 2020.

36. Cherniak DJ, Watson EB, Wark DA. Ti diffusion in quartz. Chemical Geology. 2007; 236(1–2):65–74.

37. Huang RF, Audetat A. The titanium-in-quartz (TitaniQ) thermobarometer: A critical examination and recalibration. Geochimica Et Cosmochimica Acta. 2012; 84:75–89.

38. Thomas JB, Watson EB, Spear FS, Shemella PT, Nayak SK, Lanzirotti A. TitaniQ under pressure: the effect of pressure and temperature on the solubility of Ti in quartz. Contributions to Mineralogy and Petrology. 2010; 160(5):743–59.

39. Thomas JB, Watson EB, Spear FS, Wark DA. TitaniQ recrystallized: experimental confirmation of the original Ti-in-quartz calibrations. Contributions to Mineralogy and Petrology. 2015; 169(3):27.

40. Wark DA, Watson EB. TitaniQ: a titanium-in-quartz geothermometer. Contributions to Mineralogy and Petrology. 2006; 152(6):743–54.

41. Pamukcu AS, Ghiorso MS, Gualda GAR. High-Ti, bright-CL rims in volcanic quartz: a result of very rapid growth. Contributions to Mineralogy and Petrology. 2016; 171(12):105.

42. Gualda GAR, Pamukcu AS, Ghiorso MS, Anderson AT Jr., Sutton SR, Rivers ML. Timescales of Quartz Crystallization and the Longevity of the Bishop Giant Magma Body. PLOS ONE. 2012; 7(5):e37492. https://doi.org/10.1371/journal.pone.0037492 PMID: 22666359

43. Sutton SR, Bertsch PM, Newville M, Rivers M, Lanzirotti A, Eng P. Microfluorescence and microtomography analyses of heterogeneous earth and environmental materials. Reviews in Mineralogy and Geochemistry. 2002; 49(1):429–83.

44. Zhukova I, O'Neill HS, Cambell IH, Kilburn MR. The effect of silica activity on the diffusion of Ni and Co in olivine. Contributions to Mineralogy and Petrology. 2014; 168(2):1–15.

45. Cherniak DJ. REE diffusion in olivine. American Mineralogist. 2010; 95(2–3):362–8.

46. Qian Q, O'Neill HSC, Hermann J. Comparative diffusion coefficients of major and trace elements in olivine at ~ 950˚C from a xenocryst included in dioritic magma. Geology. 2010; 38(4):331–4.

47. Jollands M, O'Neill HSC, Van Orman J, Berry A, Hermann J, Newville M, et al. Substitution and diffusion of Cr2+ and Cr3+ in synthetic forsterite and natural olivine at 1200–1500˚C and 1 bar. Geochimica et cosmochimica acta. 2018; 220:407–28.

48. Cherniak D, Watson E. Pb diffusion in zircon. Chemical Geology. 2001; 172(1):5–24.